Supporting Information for Exploring the Stability of Twisted van der Waals Heterostructures

Andrea Silva,[*,†,‡] Victor E.P. Claerbout,[*,¶] Tomas Polcar,[†,‡,¶] Denis Kramer,[†,§] and Paolo Nicolini[¶]

†*Engineering Materials, University of Southampton*

‡*national Centre for Advanced Tribology Study at University of Southampton*

¶*Advanced Materials Group, Department of Control Engineering, Faculty of Electrical Engineering, Czech Technical University in Prague (CTU)*

§*Mechanical Engineering, Helmut Schmidt University, Hamburg, Germany*

E-mail: a.silva@soton.ac.uk; claervic@fel.cvut.cz

In the following, we present in more details the methods and technical details used in this work. In the first section, we describe the protocol used to obtain the supercells of the heterostructures. We also provide a table with the parameters of all structures used in this study. In the second section, we explain the protocol used to refine the force field parameters, including the updated parameters. In the third section, we prove that the enhancement of the LJ parameters does not alter the actual physics of the problem. In the fourth section, we discuss the phonon dispersion and how we extracted from it the quantities required as input for the NM approximation. In the fifth section, we further investigate the limits of the NM theory by modelling a constrained system midway between pure NM assumptions and a fully free bilayer. Finally, in the sixth section, we present a benchmark of the force fields used.

1 Supercells for twisted lattices

Here, we explain the procedure used to obtain the twisted lattice supercells. Let l_{a} and l_{b} be the spacing of the Bravais lattices of layer a and layer b, respectively and $\hat{\mathbf{a}}_1 = \left(\begin{smallmatrix}1\\0\end{smallmatrix}\right)$ be one of the primitive versors of the first lattice, aligned with the x axis; the lattice with the desired periodicity is generated by a primitive vector, $\mathbf{a}_1 = l_{\mathrm{a}}\hat{\mathbf{a}}_1$. The matrix representing the discrete rotational symmetry of the lattice by an angle $\Omega = \pi/3$ is:

$$\underline{\underline{R}}_{\Omega} = \begin{pmatrix} \cos\pi/3 & -\sin\pi/3 \\ \sin\pi/3 & \cos\pi/3 \end{pmatrix} = \begin{pmatrix} 1/2 & -\sqrt{3}/3 \\ \sqrt{3}/3 & 1/2 \end{pmatrix} \tag{S.1}$$

thus, the second versor defining the lattice is $\hat{\mathbf{a}}_2 = \underline{\underline{R}}_{\Omega}\hat{\mathbf{a}}_1$. Since the second lattice, b, has the same symmetry but it is rotated with respect to the first one by an angle θ, versors defining it are $(\hat{\mathbf{b}}_1, \hat{\mathbf{b}}_2) = (\underline{\underline{R}}_{\theta}\hat{\mathbf{a}}_1,\ \underline{\underline{R}}_{\Omega}\underline{\underline{R}}_{\theta}\hat{\mathbf{a}}_1)$, where

$$\underline{\underline{R}}_{\theta} = \begin{pmatrix} \cos\theta & -\sin\theta \\ \sin\theta & \cos\theta \end{pmatrix} \tag{S.2}$$

describes the misalignment between the lattices. A heterostructure supercell will be compatible with both periodicities if the individual lattice cells match exactly at the edges, in other words, if the following matching condition is satisfied

$$l_{\mathrm{a}}(n_1\hat{\mathbf{a}}_1 + n_2\hat{\mathbf{a}}_2) = l_{\mathrm{b}}(m_1\hat{\mathbf{b}}_1 + m_2\hat{\mathbf{b}}_2), \tag{S.3}$$

where n_1, n_2, m_1, m_2 represent the repetition along the corresponding versor of the unit cell of the first and second lattice, respectively. An overview of the matching condition is given in Figure S1. This condition can be rewritten with a matrix formalism to:

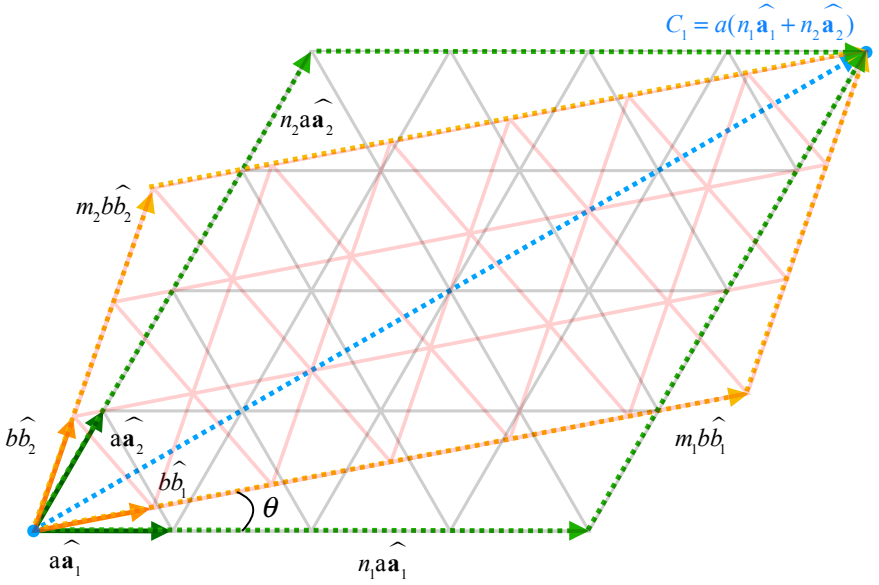

Figure S1: Graphical overview of the matching condition in Eq. (S.3) for unit cells with different lattice constants a and b at imposed angles θ. Colored arrows refer to primitive, repeated and supercell lattices, as indicated by the labels. The low-opacity lines connect the points of the Bravais lattice described by the primitive vectors.

$$\frac{l_\mathrm{a}}{l_\mathrm{b}}(n_1\hat{\mathbf{a}}_1 + n_2\underline{\underline{R}}_\Omega \cdot \hat{\mathbf{a}}_1) = m_1\underline{\underline{R}}_\theta \cdot \hat{\mathbf{a}}_1 + m_2\underline{\underline{R}}_\Omega \cdot \underline{\underline{R}}_\theta \cdot \hat{\mathbf{a}}_1$$

$$\rho \begin{pmatrix} \mathbb{I} & \underline{\underline{R}}_\Omega \end{pmatrix} \cdot \begin{pmatrix} n_1 \\ n_2 \end{pmatrix} = \begin{pmatrix} \mathbb{I} & \underline{\underline{R}}_\Omega \end{pmatrix} \cdot \begin{pmatrix} m_1 \\ m_2 \end{pmatrix} \cdot \underline{\underline{R}}_\theta \tag{S.4}$$

where $\mathbb{I}$ is the identity matrix, we used the definition of the lattice vectors, introduced the mismatch ratio $\rho = l_\mathrm{a}/l_\mathrm{b}$, grouped the matrices and the indexes in vectors and simplified $\hat{\mathbf{a}}_1$ from both sides.

Although the mismatch ratio of a system is fixed by the equilibrium values of the lattice parameters, it would be impractical to approximate a real number using integers, as the size of the supercells would easily exceed our computational capabilities. Instead, we follow instead the inverse procedure: given the four indexes $\{m_i, n_i\}_{i=1,2}$, we can invert the system and find the mismatch ratio ρ and the misalignment angle θ that satisfy the matching condition of Eq. (S.3). This means that $\{m_i, n_i\}_{i=1,2}$ are now fixed parameters of Eq. (S.3), while ρ is a variable, along with θ. Next, we find an expression for ρ and θ in terms of $\{m_i, n_i\}_{i=1,2}$ that satisfies Eq. (S.3). In the following paragraph, we address the problem of selecting sets of indices, whose corresponding ρ is close enough the real value fixed by the system ρ_0. We solve the equation Eq. (S.4) for the matrix $\underline{\underline{R}}_\theta$ and for ρ under the constraint that $\underline{\underline{R}}_\theta$ is a rotation matrix, namely:

$$\begin{cases} \underline{\underline{R}}_\theta = \rho \left(m_1\mathbb{I} + m_2\underline{\underline{R}}_\Omega\right)^{-1} \begin{pmatrix} \mathbb{I} & \underline{\underline{R}}_\Omega \end{pmatrix} \cdot \begin{pmatrix} n_1 \\ n_2 \end{pmatrix} \\ \det \underline{\underline{R}}_\theta = 1. \end{cases} \tag{S.5}$$

The first line in Eq. (S.5) is readily solved by

$$\begin{aligned}\underline{\underline{R}}_\theta &= \frac{\rho}{N_\mathrm{b}}\begin{pmatrix} m_1n_1+m_2n_2+1/2(m_1n_2+m_2n_1) & -\sqrt{3}/2(m_1n_2-m_2n_1) \\ \sqrt{3}/2(m_1n_2-m_2n_1) & m_1n_1+m_2n_2+1/2(m_1n_2+m_2n_1)\end{pmatrix} \\ &= \frac{\rho}{N_\mathrm{b}}\underline{\underline{A}}, \end{aligned} \tag{S.6}$$

where $N_\mathrm{b} = m_1^2 + m_2^2 + m_1m_2$ is the number of Bravais lattice points in the b lattice[1] and $\underline{\underline{A}}$, implicitly defined in the last step, is shorthand for the matrix of known coefficients. Substituting Eq. (S.6) into the second line of Eq. (S.5) yields an expression for ρ: $\det \underline{\underline{R}}_\theta = \frac{\rho^2}{N_\mathrm{b}^2}\det \underline{\underline{A}} = 1$. Substituting this back into Eq. (S.6) gives us the solution of (ρ, θ) of Eq. (S.3) at chosen $\{m_i, n_i\}_{i=1,2}$:

$$\begin{cases} \rho &= \frac{N_\mathrm{b}}{\sqrt{\det \underline{\underline{A}}}} \\ \theta &= (\underline{\underline{R}}_\theta)_{11} = \arccos\left(\frac{1}{\sqrt{\det \underline{\underline{A}}}}A_{11}\right) \end{cases} \tag{S.7}$$

Finally, the first vector of the supercell is given by one of the members of the equality in Eq. (S.3) and the second is obtained by symmetry, i.e.,

$$\mathbf{C_1} = l_\mathrm{a}(n_1\hat{\mathbf{a}}_1 + n_2\hat{\mathbf{a}}_2) \tag{S.8}$$

$$\mathbf{C_2} = \underline{\underline{R}}_\Omega \cdot \mathbf{C_1} = -l_\mathrm{a}n_1\hat{\mathbf{a}}_1 + l_\mathrm{a}(n_1+n_2)\hat{\mathbf{a}}_2. \tag{S.9}$$

In order to obtain a system with the desired misalignment θ, and a ρ that is an acceptable approximation of the equilibrium mismatch ρ_0, we consider all combinations of integers $n_i,\ m_i$ within the range $(-200, 200)$ and select the supercells which satisfy $\theta \in [0°, 60°]$ and $|\Delta\rho| = |\rho - \rho_0| \leq 1 \times 10^{-7}$. We then bin the resulting supercells with a spacing of $\Delta\theta = 0.01°$ and select the cell with the fewest Bravais points within each bin. Note that this procedure does not guarantee that the resulting supercells will be evenly spaced with respect to the

[1] An equivalent relation holds for the other lattice $N_\mathrm{a} = n_1^2 + n_2^2 + n_1n_2$

mismatch angle.

The indices defining the supercells used in this work for the MoS_2/G heterostructures are reported in Table S1, along with the misalignment angle, $\rho - \rho_0$, and the number of atoms in each layer. For this system, $\rho_0 = l_G/l_{MoS_2} = 2.460\,187\,8\,\text{Å}/3.093\,682\,7\,\text{Å} = 0.7952295$, and the number of atoms in each lattice is given by the number of Bravais lattice points multiplied by the number of atoms in the crystal basis, i.e. $N_{tot} = N_{Bravais} \cdot n_{basis}$ with n_{basis} is equal to 2 and 3 for G and MoS_2, respectively. In creating the supercell, the strain ϵ due to the approximated mismatch ρ is applied to MoS_2. The residual strains for different values of the tolerance $\Delta\rho = \rho - \rho_0$ are reported in Figure S2.

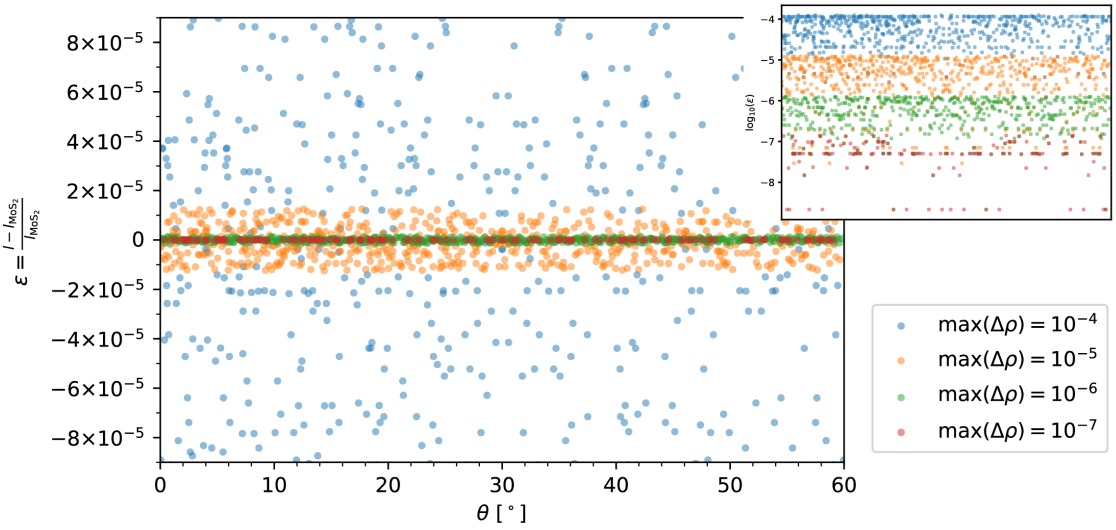

Figure S2: Strain applied to the MoS_2 lattice versus angle imposed to the supercell according to Eq. (S.7) for different values of tolerance. The tolerance value used in the work is $\Delta\rho \leq 1 \times 10^{-7}$. The lattice spacing is obtained as $l = l_G/\rho$, where ρ is the solution of the Eq. (S.7). The inset in the upper right corner reports the logarithm of the absolute value of the strain ϵ .

$\theta[^\circ]$	n_1	n_2	m_1	m_2	$\rho - \rho_0$	N_G	N_{MoS_2}
0.23	**-135**	**-104**	**-108**	**-82**	**9.8e-08**	**86162**	**81732**
0.58	-192	61	-153	50	8.1e-08	57744	54774
0.79	-184	-41	-148	-30	9.8e-08	86162	81732
1.01	-113	-182	-86	-148	-6.2e-08	132916	126081

1.24	-176	-59	-137	-51	4.3e-09	89682	85071
1.39	-109	39	-87	33	-5.7e-08	18300	17361
1.60	-141	-128	-107	-107	2.6e-08	108626	103038
2.11	-138	-99	-104	-85	-2.2e-08	85012	80640
2.88	-184	-41	-140	-42	9.8e-08	86162	81732
3.05	-118	12	-96	15	9e-08	25302	24000
3.21	-182	-113	-134	-102	-6.2e-08	132916	126081
4.17	-184	33	-142	15	8.1e-08	57744	54774
4.93	-191	-48	-140	-55	3.5e-08	95904	90972
5.30	-192	61	-155	62	8.1e-08	57744	54774
5.34	-185	63	-149	63	4.6e-08	53076	50349
5.95	-164	-41	-118	-50	1.5e-08	70600	66969
6.23	-164	-115	-110	-113	6.2e-08	117960	111894
6.64	-123	-185	-71	-169	-8.8e-08	144216	136800
6.75	-164	-145	-154	-89	4.4e-08	143402	136029
7.18	-152	-99	-140	-55	3.5e-08	95906	90972
7.94	-172	169	-146	122	-8.3e-08	58152	55164
8.14	-118	12	-99	24	9e-08	25302	24000
8.42	-163	-125	-156	-68	-9.6e-08	125136	118704
8.64	-145	145	-104	124	1.2e-08	42048	39885
8.75	-138	-99	-85	-104	-2.2e-08	85012	80640
9.01	-184	33	-153	50	8.1e-08	57744	54774
9.04	-176	-59	-117	-76	4.3e-09	89682	85071
9.69	-172	169	-122	146	-8.3e-08	58152	55161
9.75	**-181**	**-95**	**-113**	**-110**	**6.2e-08**	**117960**	**111894**
10.25	-169	-174	-90	-178	7e-08	176484	167409
10.64	-181	-95	-110	-113	6.2e-08	117960	111894

10.81	-164	-145	-89	-154	4.4e-08	143402	136029
11.22	-174	-169	-90	-178	7e-08	176484	167409
11.37	-170	71	-130	31	-4.5e-08	43740	41493
12.17	-113	-182	-134	-102	-6.2e-08	132916	126081
12.27	-185	63	-138	19	4.6e-08	53076	50349
12.60	-192	61	-142	15	8.1e-08	57744	54774
12.99	-135	-104	-140	-42	9.8e-08	86162	81732
13.65	-118	12	-81	-15	9e-08	25302	24000
13.73	-184	33	-155	62	8.1e-08	57744	54774
14.52	-144	-98	-150	-31	1.7e-10	88904	84333
15.20	-184	33	-127	-15	8.1e-08	57744	54774
15.53	-185	63	-149	86	4.6e-08	53076	50349
15.63	-184	-41	-108	-82	9.8e-08	86162	81732
16.39	-182	-113	-86	-148	-6.2e-08	132916	126081
16.66	-135	-104	-148	-30	9.8e-08	86162	81732
17.14	-163	-125	-68	-156	-9.6e-08	125136	118704
17.26	-109	39	-87	54	-5.7e-08	18300	17358
18.47	-192	61	-155	93	8.1e-08	57744	54774
18.74	-118	12	-75	-24	9e-08	25302	24000
18.91	-41	-184	30	-178	9.8e-08	86162	81729
19.89	**-185**	**-123**	**-71**	**-169**	**-8.8e-08**	**144216**	**136800**
20.15	-184	-23	-101	-79	-7.1e-08	77232	73263
20.95	-187	-101	-75	-153	-5.7e-08	128114	121527
21.08	-152	-99	-55	-140	3.5e-08	95906	90972
21.47	-182	-23	-173	48	-8.3e-08	75678	71784
21.55	-135	-104	-42	-140	9.8e-08	86162	81732
22.24	-170	71	-130	99	-4.5e-08	43740	41493

22.58	-184	-41	-182	42	9.8e-08	86162	81732
23.03	-176	-59	-76	-117	4.3e-09	89682	85071
23.20	-192	61	-153	103	8.1e-08	57744	54774
23.63	-192	61	-127	-15	8.1e-08	57744	54774
24.25	-148	-132	-185	-15	-4.9e-08	117728	111675
24.67	-184	-41	-82	-108	9.8e-08	86162	81732
25.00	-113	-182	-174	-52	-6.2e-08	132916	126081
25.23	-135	-104	-30	-148	9.8e-08	86162	81732
26.82	-191	-48	-195	55	3.5e-08	95904	90972
26.86	-185	63	-119	-19	4.6e-08	53076	50349
27.05	-144	-98	-31	-150	1.7e-10	88904	84333
27.74	-164	-41	-168	50	1.5e-08	70600	66969
28.03	-148	-132	-15	-185	-4.9e-08	117728	111675
28.22	-184	-23	-79	-101	-7.1e-08	77232	73263
28.37	-184	33	-103	-50	8.1e-08	57744	54774
29.17	**-176**	**-59**	**-188**	**51**	**4.3e-09**	**89682**	**85071**
30.83	-176	-59	-51	-137	4.3e-09	89682	85071
31.63	-184	33	-153	103	8.1e-08	57744	54774
31.78	-23	-184	79	-180	-7.1e-08	77232	73260
31.97	-148	-132	-200	15	-4.9e-08	117728	111675
32.26	-164	-41	-50	-118	1.5e-08	70600	66969
32.95	-144	-98	-181	31	1.7e-10	88904	84333
33.14	-185	63	-138	119	4.6e-08	53076	50349
34.77	-104	-135	30	-178	9.8e-08	86162	81729
35.33	-41	-184	82	-190	9.8e-08	86162	81729
35.75	-148	-132	15	-200	-4.9e-08	117728	111675
36.37	-192	61	-142	127	8.1e-08	57744	54774

36.80	-192	61	-103	-50	8.1e-08	57744	54774
36.97	-59	-176	76	-193	4.3e-09	89682	85068
37.42	-184	-41	-42	-140	9.8e-08	86162	81732
37.76	-170	71	-99	-31	-4.5e-08	43740	41493
38.45	-135	-104	-182	42	9.8e-08	86162	81732
38.53	-23	-182	-125	-48	-8.3e-08	75678	71784
38.92	-152	-99	-195	55	3.5e-08	95906	90972
39.85	-23	-184	101	-180	-7.1e-08	77232	73260
41.09	-184	-41	-30	-148	9.8e-08	86162	81732
41.26	-118	12	-99	75	9e-08	25302	24000
41.53	-192	61	-93	-62	8.1e-08	57744	54774
42.74	-109	39	-54	-33	-5.7e-08	18300	17361
43.34	-135	-104	30	-178	9.8e-08	86162	81729
44.37	-41	-184	108	-190	9.8e-08	86162	81729
44.47	-185	63	-86	-63	4.6e-08	53076	50349
44.80	-184	33	-142	127	8.1e-08	57744	54774
45.48	-144	-98	31	-181	1.7e-10	88904	84333
46.27	-184	33	-62	-93	8.1e-08	57744	54774
46.35	-118	12	-96	81	9e-08	25302	24000
47.01	-135	-104	42	-182	9.8e-08	86162	81732
47.40	-192	61	-127	142	8.1e-08	57744	54774
47.73	-185	63	-119	138	4.6e-08	53076	50349
48.63	-170	71	-99	130	-4.5e-08	43740	41493
50.31	-172	169	-146	24	-8.3e-08	58152	55164
50.99	-184	33	-50	-103	8.1e-08	57744	54774
51.20	-104	-135	82	-190	9.8e-08	86162	81729
51.25	-138	-99	-189	85	-2.2e-08	85012	80640

51.36	-145	145	-124	20	1.2e-08	42048	39885
51.86	-118	12	-24	-75	9e-08	25302	24000
52.06	-172	169	-24	146	-8.3e-08	58152	55161
52.82	-152	-99	55	-195	3.5e-08	95906	90972
54.05	-164	-41	-168	118	1.5e-08	70600	66969
54.66	-185	63	-63	-86	4.6e-08	53076	50349
55.07	-191	-48	-195	140	3.5e-08	95904	90972
55.83	-184	33	-127	142	8.1e-08	57744	54774
56.95	-118	12	-15	-81	9e-08	25302	24000
57.12	-184	-41	-182	140	9.8e-08	86162	81732
57.89	-138	-99	-189	104	-2.2e-08	85012	80640
58.61	-109	39	-33	-54	-5.7e-08	18300	17358
58.76	-176	-59	-188	137	4.3e-09	89682	85071
59.21	-184	-41	30	-178	9.8e-08	86162	81729
59.42	-192	61	-50	-103	8.1e-08	57744	54774
59.77	-135	-104	82	-190	9.8e-08	86162	81729

Table S1: Parameters of the rotated supercells used in this work. The lines relative to the four misaligned geometries shown in Figure 5 in the main text are highlighted in bold font.

2 Force Field refinement

As part of this study, we refined the LJ coupling parameters for the heterostructure of MoS_2 and G. As a starting point, we took the parameters provided in Ref.[1] However, our preliminary results revealed some significant discrepancies, both quantitatively as well as qualitatively, with the results obtained via accurate DFT calculations. This motivated us to perform a recalibration of the parameters.

In order to do so, we applied the Simplex algorithm[2] as implemented in SciPy.[3] This

algorithm samples the N-dimensional (N=number of LJ parameters) phase space using a convex polygon. This algorithm acts on the following objective function:

$$\chi^2[f_{\mathrm{L}}] = \frac{1}{W}\int_0^{\infty} |f_{\mathrm{DFT}}(r) - f_L(r)|^2 w(r)\mathrm{d}r \tag{S.10}$$

$$\approx \frac{1}{W}\sum_{r_i}^{r_{\mathrm{cut}}} |f_{\mathrm{DFT}}(r_i) - f_L(r_i)|^2 w(r_i), \tag{S.11}$$

where $r_{\mathrm{cut}} = 14.5\,\text{Å}$, beyond the LJ potential cutoff in LAMMPS and enough to consider negligible the LJ interactions in VASP. The function f_{DFT} is the reference, in our case the Lennard-Jones binding energy profile from DFT, whereas f_{L} is the same binding energy profile computed with LAMMPS using the current ϵ and σ. We used the weight function $w(r) = \exp[-(\frac{r-r_0}{\zeta})^2]$ to ensure that the most relevant part, the minimum of the Lennard-Jones at $r_0 = 4.94\,\text{Å}$ and its directs surroundings, are represented correctly. The amplitude of the relevant interval around the minimum is tuned with the ζ parameter. Both the reference energy profile and the one from LAMMPS are obtained by fixing the interlayer distance between G and MoS_2. In our case we fixed the carbon atoms and the outermost sulfur atoms in the z direction. The heterostructure itself results from a 4x4 MoS_2 unit cell repetition and a 5x5 G unit cell repetition, in which the residual strain of 2.6% is applied to MoS_2. The results of this optimization can be found in Table S2 and Figure S3.

Table S2: Optimized LJ parameters for the interlayer interaction between G and MoS_2.

Optimized LJ Parameters			
Atoms	ϵ [meV]	σ [Å]	ζ [Å]
C-S	1.64	3.640	0.30
C-Mo	4.55	4.391	0.30

3 LJ enhancement

The LJ-coupling between the layers of MoS_2 and G was enhanced during the constraint simulations as mentioned in the main text. This was done because the strain posed on the

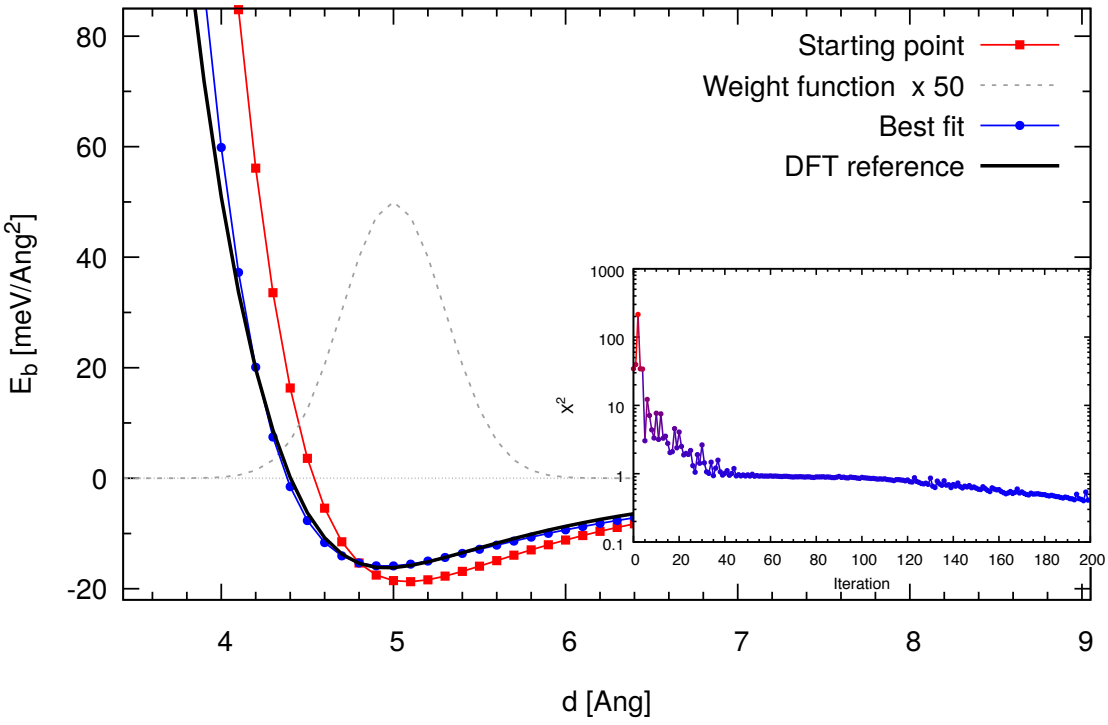

Figure S3: Refining of LJ-parameters. Binding energies (normalized by the cell area) versus the interlayer distance in $\AA$. The black line is the reference binding energy obtained through DFT, whereas the red and the blue line are the starting and final binding energies obtained through LAMMPS, respectively. The dashed line represents the weight function around the energy minimum enhanced by a factor of 50, as guide for the eye. The inset shows the objective function χ^2 versus the number of the iterations of the optimization algorithm.

MoS_2 lattice, in order to create a supercell suitable for the application of PBC, results in a noise significantly affecting the energy profile upon rotating the lattices. In Figure S4, we report the underlying energy profile $E(\theta)$ for different values of the scaling factor f in $\epsilon' = f\epsilon$. From Figure S4, it can be seen that this computational trick does not alter the physics, but purely amplifies the energy trends that otherwise get progressively hidden by the noise. Figure S5 reports the scaling relation at $\theta = 30°$, showing an almost quadratic behaviour. In order to make comparison between Fig. 1 and Fig. 2 in the main text easier, we scaled back the value computed at $\epsilon'_{LJ} = 100\epsilon_{LJ}$ according to $E^{100}(30°)/E^{1}(30°) = 1751.57$. In other words, both the minima and maxima remain located at the same angle, however, their absolute energy value is scaled according to the LJ-coupling.

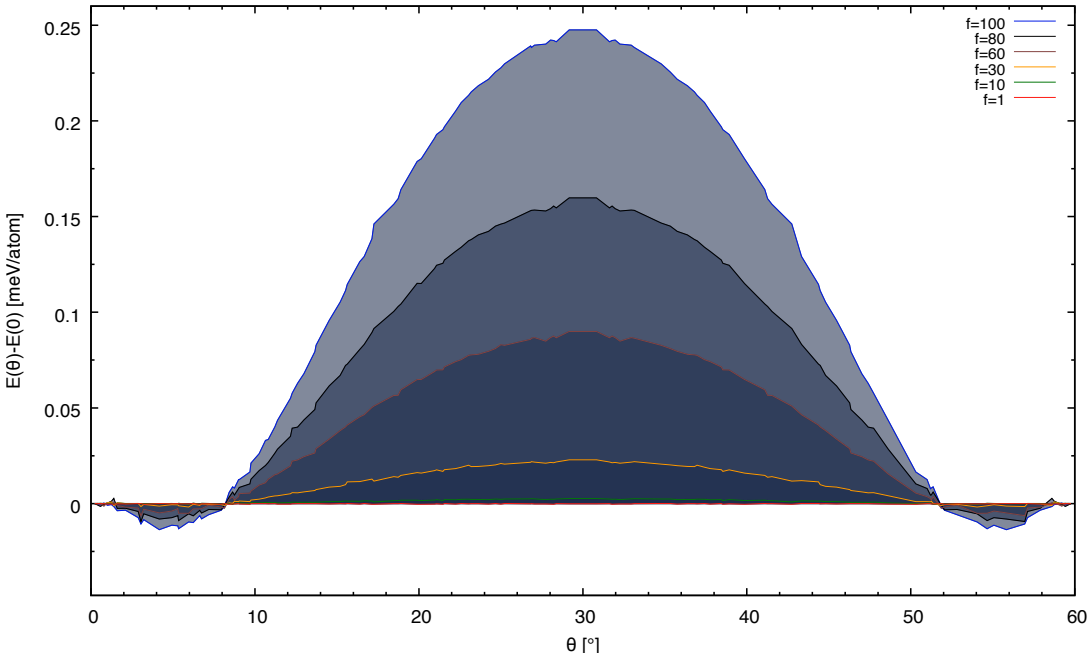

Figure S4: Enhancement of the LJ-coupling. The plot reports the energy $E(\theta)$ in meV/atom versus angle θ for rigid MoS_2 and soft G for increasing values of LJ coupling f, as reported in the legend.

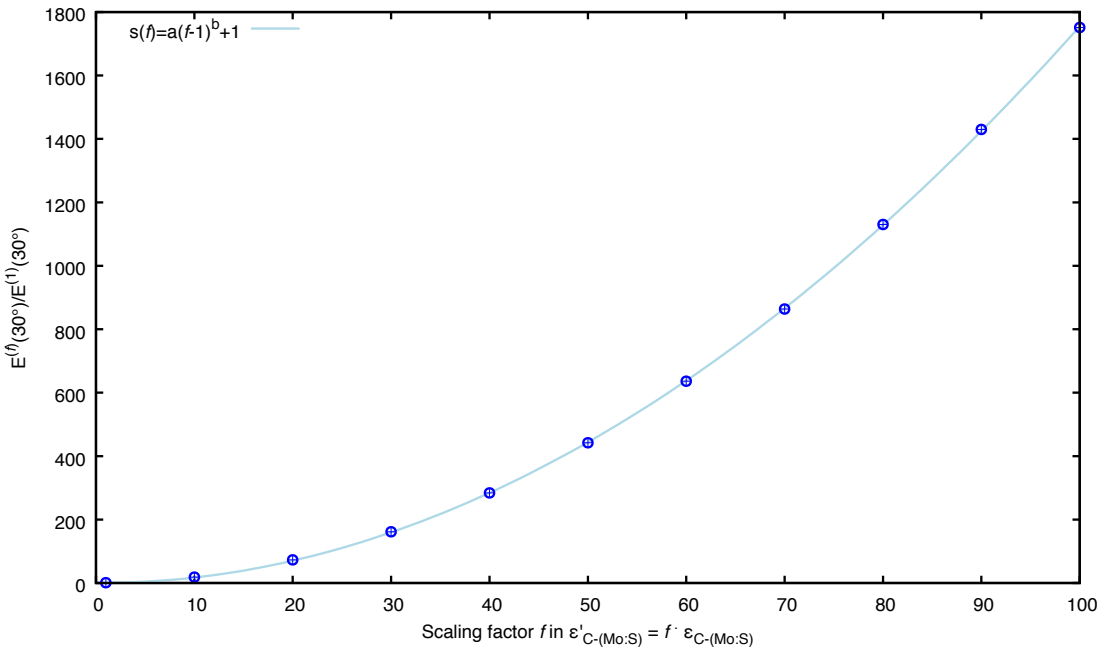

Figure S5: Scaling relation between the maximum energy ratio and the LJ coupling parameter ϵ. Blue circles represent the energy at $\theta = 30°$ computed at a given enhancement factor f, with respect to $f = 1$, versus the scaling factor f. The light-blue line shows the fitted power law reported in the legend with parameters $a = 0.217837$ and $b = 1.9572$.

4 Phonon dispersion and sound velocity

Figure S6 reports the phonon band structure along the path $\Gamma \to M \to K \to \Gamma$ of G and MoS_2, panels (a) and (b) respectively. These figures allow us to compare phonon dispersion computed from quantum forces, at the DFT level, and from classical forces. We focus on the acoustic modes first. Quantum and classical dispersion are in good agreement around Γ, the center of the Brillouin zone; this means that the long wavelength distortions at the base of NM theory are well-described by the classical force fields. As we move to the edge of the cell, towards shorter distortions, the two dispersions start to deviate. For example, the splitting of quantum-computed transverse and longitudinal branches observed at M point in G is shifted to a different k in the classical results. Similar observations can be made for the region around K and for the MoS_2 phonon bands. The general trend is that the classical treatment underestimates the energy of acoustic branches and overestimates

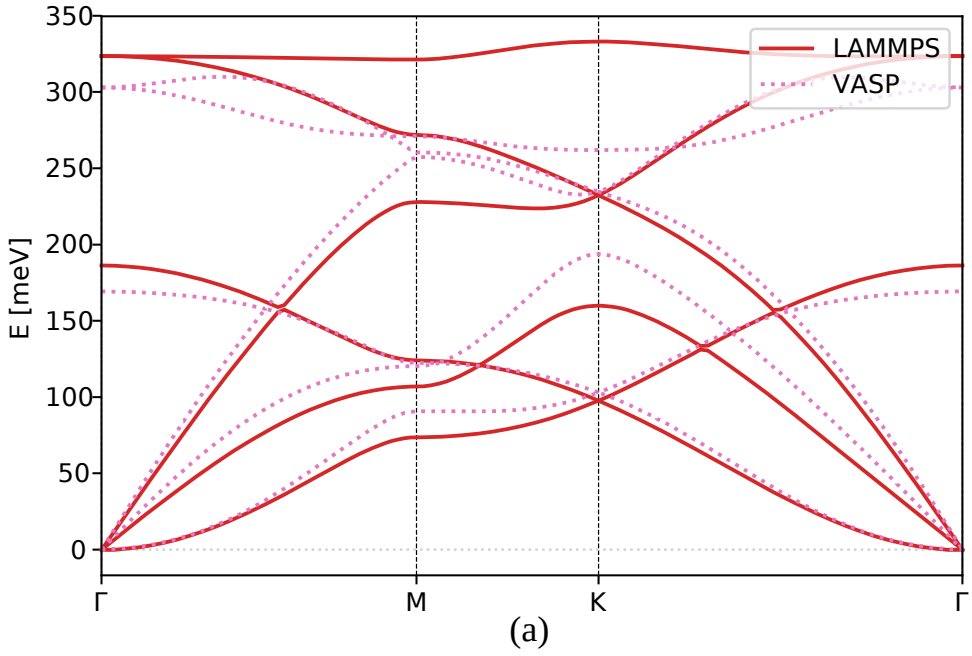

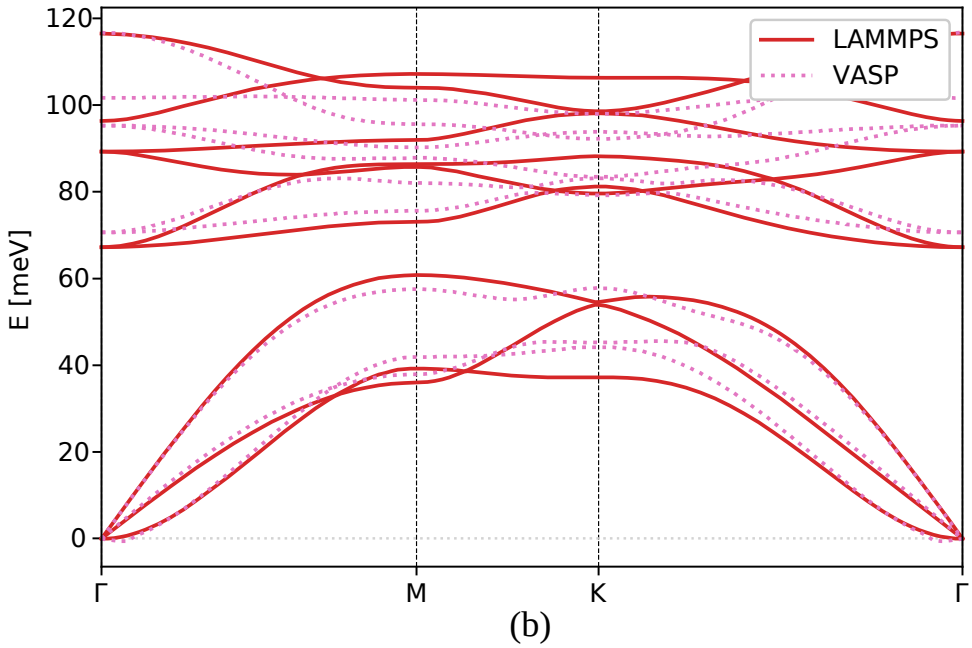

Figure S6: Phonon band structure of (a) G and (b) MoS_2 computed with LAMMPS (solid lines) and VASP (dashed lines). The y axis reports the phonon energy, while the x axis marks the distance from the origin along the path $\Gamma \to M \to K \to \Gamma$.

the optical ones. However, strong quantitative agreement is not needed for the qualitative statements developed in the main text and, in order to obtain the sound velocity needed as input of the NM theory, only an accurate description around the Γ point is required.

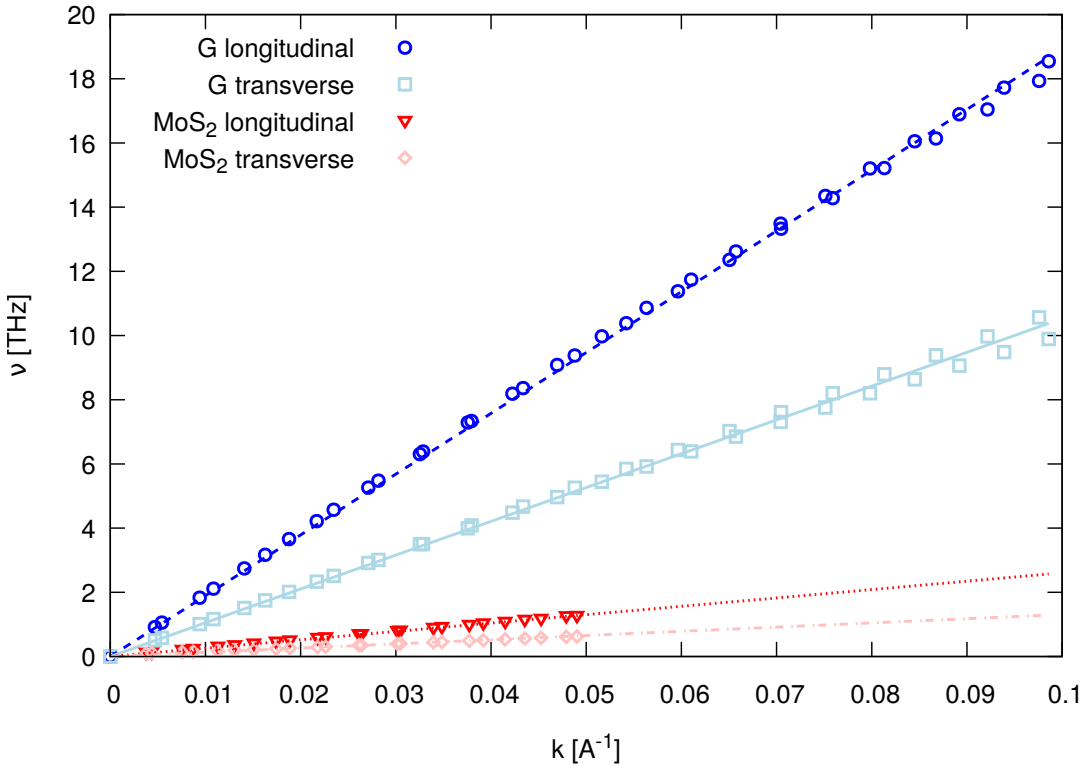

Figure S7: Sound velocity fit from the phonon dispersion in G (shades-of-blue symbols) and MoS_2 monolayer (shades-of-red symbols). The y axis reports the frequency ν in THz and the x axis the distance from Γ in $Å^{-1}$. The color-matching lines report the linear fit of that branch, i.e. $\nu_i = v_i k$.

As explained in the main text, the NM theory describes the distortion of a 2D layer due to interaction with a rigid substrate in terms of long wavelength phonons. The theory yields analytical predictions in the limit of linear dispersion $\omega_i(k) = v_i k$, where $i = \mathrm{L}, \mathrm{T}$ labels either the transverse (T) or longitudinal (L) branch and v_i is the speed of sound of the corresponding branch i. This is defined as the slope of the phonon dispersion near Γ: $v_i = \left.\frac{\partial \omega(k)}{\partial k}\right|_\Gamma$. Figure S7 shows the longitudinal and transverse branches close to Γ of G and MoS_2. The plot also shows the linear fits obtained from the points, including their fitted

slopes representing the sound velocities, as reported in Table S3. This leads to the values

Table S3: Sound velocity of transverse and longitudinal phonon branches in G and monolayer MoS_2 extracted from Figure S7. The uncertainty arises from the linear fitting procedure.

Material	v_L[km/s]	v_T[km/s]
G	18.9403 ± 0.0005	10.5298 ± 0.0005
MoS_2	0.2608 ± 0.0005	0.131 ± 0.002

$\delta_{\mathrm{G}} = 2.235$ and $\delta_{\mathrm{MoS_2}} = 2.968$ used to evaluate Eq. 4 in the main text.

5 NM approximation limits

We discuss the difference behaviour between the pure NM theory reported the main text (see Figure 2 in the main text) and free 2D system. More specifically, we consider a bilayer MoS_2/G where atoms are free to move in the xy plane but the z coordinate of each atom is frozen. This corresponds to lifting the rigid substrate assumption of the NM theory, while enforcing a constant interlayer distance. Figure S8 reports on the results for this case. The NM theory does not cover this scenario, as here none of the two layers is rigid. As a result, the two layers can mutually influence and distort each other, reaching configurations not included in the NM model. A minimum at $\theta \approx 8°$ is clearly visible, midway between the two rigid substrate approximations. This means that the physics described in the NM theory still applies to this case, even though the model does not describe the mutual interaction between the layers and does not provide a prediction for the the minimum-energy angle. The behaviour of the system is thus qualitatively different from the h-BN/G heterostructures studied by Guerra et al.[4] In that case the NM theory was found to explain quantitatively the energetics of the rigid and z-frozen scenario, i.e. blue and red lines in Figure S8, but removing the rigid substrate constraint changed the behavior qualitatively: the non-zero minimum-energy angle predicted by NM disappeared from the energy profile of the system. From this observation, we can conclude that in our system, comprising of 2D and 3D ML, when the assumption of a rigid substrate is relaxed, a non-zero minimum angle dominates

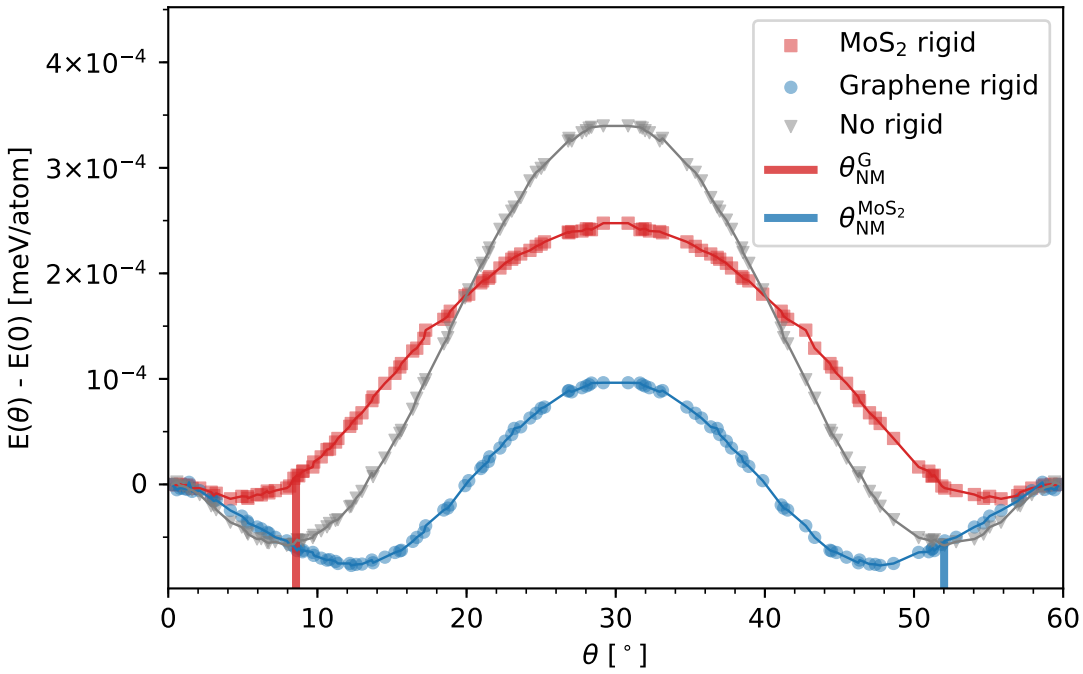

Figure S8: Energy per atom $E(\theta)$, in meV/atom, as a function of the imposed angle θ in degrees for different 2D models: red squares refer to flexible G on top of rigid MoS_2; blue circles refer to flexible MoS_2 on top of rigid G. Gray triangles refer to flexible MoS_2 on top of flexible G. The reference value of the energy scale is set by $E(0)$ and the values have been corrected according to the initial LJ enhancement. Red and blue segments mark the minimum angle predicted by the NM theory for the first and second case, respectively.

the energy landscape and, thus, the NM argument still describes the physics of the system.

6 Force Field Benchmark

In this section, we present a benchmark of the force fields used in this study compared to experimental results and first principle calculations.

Table S4: Structural parameters obtained by authors using the SW model for MoS_2, the REBO model for graphene together with reference data from X-ray diffraction experiments and density functional theory (DFT) calculations. The DFT results were obtained using the following previously mentioned computational details.

	SW	REBO	DFT	Experimental
Lattice constant graphene(Å)	-	2.4602	2.4668	2.4589,[5] 2.464(2)[6]
Lattice constant MoS_2 (Å)	3.0937	-	3.1901	3.15,[7] 3.1625[8]
C-C bond distance (Å)	-	1.4204	1.4242	-
Mo-S bond distance (Å)	2.3920	-	2.4112	-

7 Magnitude of the out-of-plane displacements

In this section we compared the out-of-plane displacements of G layer with the MoS_2 one. The thickness of a ML is defined as $\tau(\theta) = z_{\max} - z_{\min}$ in the relaxed geometry. In the case of MoS_2 since it comprises 3 atomic layers, the analysis has been carried out on the separate components: bottom S layer, Mo layer and top S layer, as reported in Figure S9. The bottom S layer of MoS_2, being the closest to G, shows the larger displacements and shows an opposite trend compared to G. This is due to the fact that the less convenient it becomes for G do modulate, the more important is the contribution from the MoS_2 modulation; albeit still small if compared to the G signal. The Mo layer shows an appreciable modulation only after $\theta = 20°$, when G starts to flatten. Finally, the top S layer, furthest from the interface with G, remains essentially flat throughout the spectrum and the small fluctuations can be regarded as numerical noise.

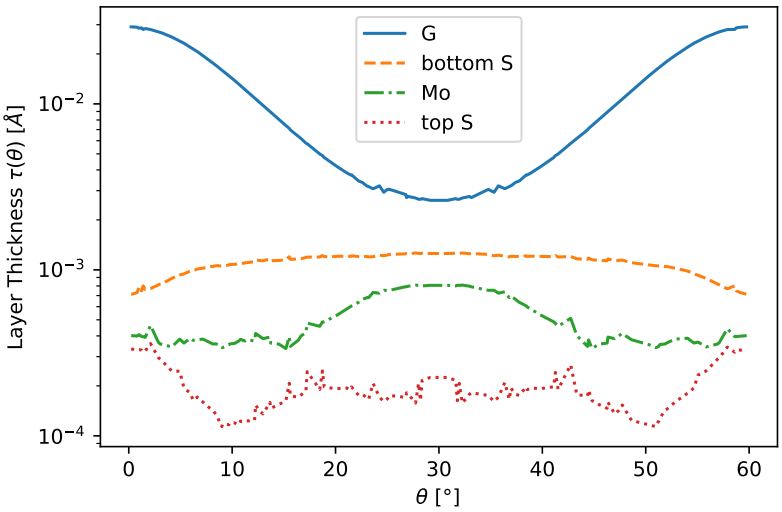

Figure S9: Thickness of the atomic layers as a function of the mismatch angle. The y axis is reported in logarithmic scale for better comparison.

The total variations Δ between all values θ are reported in Table S5. The last column reports the variations with respect to the one occurring in G (Δ_G): the modulation in MoS_2 is at least 2 orders of magnitude less than in G, thus supporting our claim that the structural distortion representing the leading order in lowering the energy occurs in the G layer only.

Table S5: Minimum and maximum thickness across θ. Variation of thickness $\Delta = \max_\theta(\tau) - \min_\theta(\tau)$. Variation relative to the one occurring in G.

Atom layer	$\min_\theta(\tau)$ [Å]	$\max_\theta(\tau)$ [Å]	Δ [Å]	Δ/Δ_G
G	0.0026	0.0291	0.0265	1
Bottom S	0.0007	0.0013	0.0006	0.021
Mo	0.0003	0.0008	0.0005	0.018
Top s	0.0001	0.0004	0.0002	0.009

References

(1) Ding, Z.; Pei, Q. X.; Jiang, J. W.; Huang, W.; Zhang, Y. W. Interfacial Thermal Conductance in Graphene/MoS_2 Heterostructures. *Carbon* **2016**, *96*, 888–896.

(2) Nelder, J. A.; Mead, R. A Simplex Method for Function Minimization. *The Computer Journal* **1965**, *7*, 308–313.

(3) Oliphant, T. E. SciPy: Open Source Scientific Tools for Python. 2007; `http://www.scipy.org/`.

(4) Guerra, R.; van Wijk, M.; Vanossi, A.; Fasolino, A.; Tosatti, E. Graphene on h-BN: to Align or Not to Align? *Nanoscale* **2017**, *9*, 8799–8804.

(5) Baskin, Y.; Meyer, L. Lattice Constants of Graphite at Low Temperatures. *Physical Review* **1955**, *100*, 544.

(6) Trucano, P.; Chen, R. Structure of Graphite by Neutron Diffraction. *Nature* **1975**, *258*, 136–137.

(7) Wakabayashi, N.; Smith, H. G.; Nicklow, R. M. Lattice Dynamics of Hexagonal MoS_2 Studied by Neutron Scattering. *Physical Review B* **1975**, *12*, 659–663.

(8) Py, M. A.; Haering, R. R. Structural Destabilization Induced by Lithium Intercalation in MoS_2 and Related Compounds. *Canadian Journal of Physics* **1983**, *61*, 76–84.